Supplementary Information for Manuscript : Ion Sensing based on Frequency-Dependent Physico-Chemical Processes at Electrode/Electrolyte Interfaces

1 Mean-Field Model: Detailed Description

This section provides a comprehensive description of the numerical mean-field model and its implementation in Matlab, offering sufficient detail for reproducing the results presented in the main text. The model builds upon the framework developed by Kopper and Doblhoff-Dier [1].

Starting with the ion distribution, we used the following expression for entropy density, to include the effect of ion size, based on lattice gas model.

$$S[c_i(x)] = -k_B \sum_{i=1}^{p} \frac{c_i \ln c_i(x)}{c_{max}} - k_B \left(c_{max} - \sum_{i=1}^{p} c_i(x) \right) \ln \left(1 - \sum_{i=1}^{p} \frac{c_i(x)}{c_{max}} \right) \tag{1}$$

where c_{max} is the maximum ion density, determined by the hydration shell size of the ions.

From the free energy in Eq. 1, an expression for the local ion concentration, $c_i(x, \phi(x), \psi(x))$, as a function of local electric and external potential can be derived by setting $\frac{d\mathcal{F}}{dc_i} = 0$:

$$c_i(x) = \frac{c_i^0 e^{-\frac{z_i \phi(x) + \psi_i(x)}{k_B T}}}{1 - \sum_{i=1}^{p} \frac{c_i^0}{c_{max}} \left(1 - e^{-\frac{z_i \phi(x) + \psi_i(x)}{k_B T}} \right)} \tag{2}$$

where c_i^0 is the bulk concentration of species i. By minimizing the free energy $\mathcal{F}$ with respect to $\phi(x)$ and inserting Eq. 2, the modified Poisson-Boltzmann equation is obtained:

$$\nabla \left(\epsilon_r \nabla \phi(x) \right) + 4\pi \sum_{i=1}^{p} z_i c_i(\phi(x)) = 0 \tag{3}$$

This second-order differential equation is solved in a 1D approximation by rewriting it as a system of coupled first-order differential equations as follow:

$$\begin{pmatrix} \phi \\ \psi \end{pmatrix} = \begin{pmatrix} \psi \\ -\frac{1}{\epsilon(\phi)} \left(\rho(x) + \frac{d\epsilon(\phi)}{d\phi} \psi^2 \right) \end{pmatrix} \tag{4}$$

These equations are solved as a boundary value problem in Matlab using the ‘bvp5c‘ function. The boundary conditions are set as $\phi(0) = V_0$, with the second boundary L positioned far enough in the solvent to ensure $\left. \frac{d\phi}{dx} \right| = 0$.

1.1 Relative Permittivity

To model the relative permittivity of interfacial water, we adapted the water molecule orientation data provided by Le *et al.* [2] to align with values reported in the literature. This approach involves extracting the probability distribution profiles for water molecule orientation and interpolating them over a potential range from -1 V to 1 V to capture the variation in molecular orientation in response to the applied electric field.

Given this orientation data, the polarization of water molecules parallel to the electric field can be calculated. The probability distributions of the angle ϕ (between the O-H bond and the surface normal) and θ (between the bisector of the water molecule and the surface normal) interpolated and the parallel polarization component P is calculated as the product of the polarization components in the θ and ϕ directions:

$$P_\theta = \int_0^{180} p_\theta \sin(\theta) \, d\theta, \tag{5}$$

$$P_\phi = \int_0^{180} p_\phi \sin(\phi) \, d\phi, \tag{6}$$

$$P = P_\theta \cdot P_\phi \tag{7}$$

In these equations, p_θ and p_ϕ represent the polarization and the probability distributions of the angles θ and ϕ, respectively. the susceptibility calculated as follow:

$$\chi = \frac{dP}{dE} \tag{8}$$

It has been considered that the electric field is uniform in the first interfacial layer, thus we can express the electric field E as:

$$E = \frac{V}{d}$$

where V is the applied potential and d is the distance in the interfacial layer. With this assumption, the equation for polarization susceptibility χ from equation 8 can be transformed to:

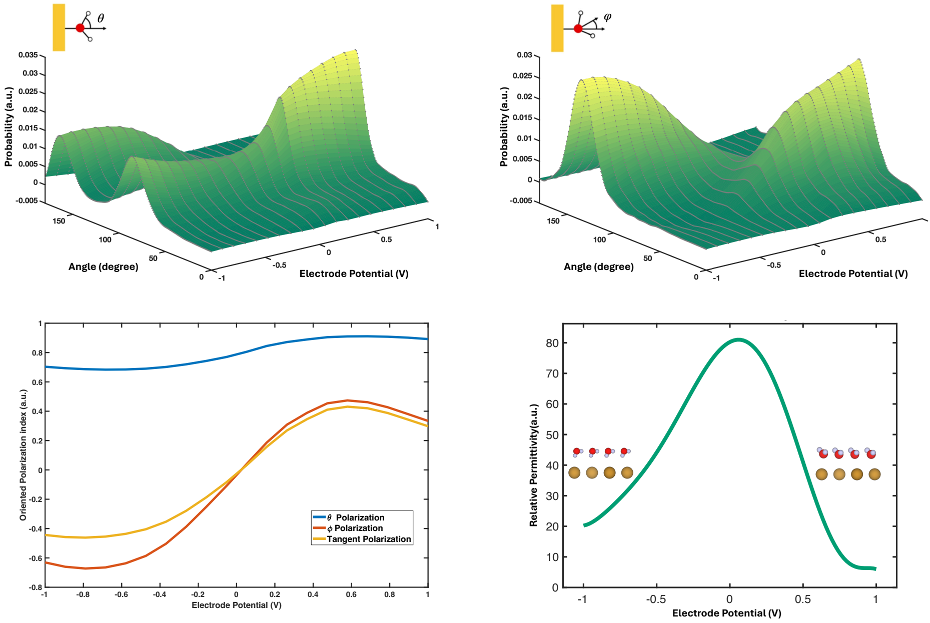

Fig. 1 Probability distribution profiles of the angle ϕ (a) between the O–H bond of water and the surface normal of the interface, and the angle θ (b) between the bisector of water and the surface normal of the interface at various applied potentials (adapted from [2]). (c) Calculated dielectric polarization parallel to the electric field, and (d) potential-dependent relative permittivity of interfacial water molecules.

$$\chi = \frac{dP}{dV}$$

The relative permittivity ϵ_r is calculated as follows:

$$\epsilon_r = 1 + \chi \tag{9}$$

To match the desired range for the relative permittivity, the values are adapted such that the maximum value is 80 and the minimum is 1. This adaptation ensures that the relative permittivity stays within the physically meaningful limits while still reflecting the changes in susceptibility χ due to the applied electric field.

In general, relative permittivity decreases under higher electric potentials, with a slower decrease in the negative direction, due to the stability of the one-H-down water structure.

1.2 Ion-Surface Interaction

Ion interaction $\psi(x)$ with the interface can be modeled with either a purely repulsive function or with a combination of attractive and repulsive terms. Here, only the repulsive Helmholtz layer interaction is considered, represented by an exponential function:

$$\psi_{rep} = k_B T e^{\frac{x_{rep} - x}{\delta_{rep}}} \tag{10}$$

where k_B is the Boltzmann constant, T is the temperature, and x_{rep} represents the thickness of the Helmholtz layer. The repulsive function generates a smooth, box-like region near the interface where ions are depleted. Based on the findings of Shin *et al.* [3], the thickness of the Helmholtz layer, denoted as x_{rep}, decreases with increasing electrode surface charge, a trend particularly pronounced for anions. This model incorporates their results, and Figure 2 illustrates the relationship between x_{rep} and electric potential. For cations, the Helmholtz layer thickness decreases as the electrode potential becomes more cathodic. At low cathodic potentials, x_{rep} begins at the radius of the cation's hydration shell. As the potential increases, the hydration shell becomes compressed, and x_{rep} approaches the minimum distance to the electrode, where the hydration shell is significantly disturbed.

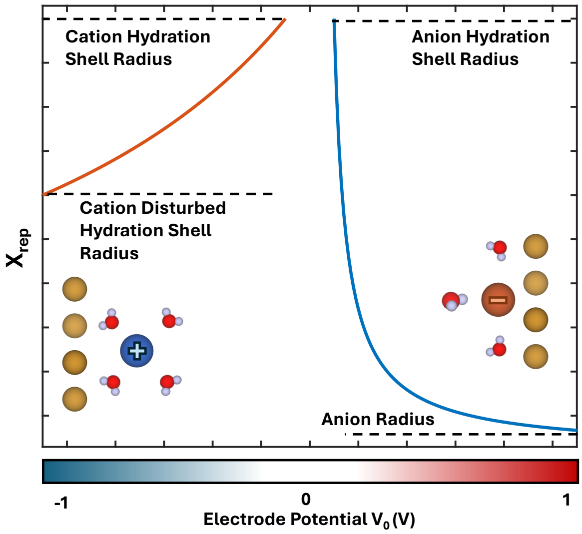

Fig. 2 Modeled Helmholtz layer thickness profile based on [3]

For anions, the Helmholtz layer thickness also decreases with increasing anodic potential. Starting from the anion's hydration shell size at lower potentials, x_{rep} reduces to the bare ion size as the potential becomes more anodic.

While ion-surface interactions are influenced by various complex factors—such as chemical bonding, image charge interactions, and the interaction of the solvation shell with the electrode surface—this model simplifies these effects to focus on the dominant trends.

1.3 Model Validation

To validate the mean-field model, the simulated ion distribution and electric field profiles are analyzed in detail. Figure 3 presents the simulated ion distribution profiles as a function of the distance from the electrode, shown on a logarithmic scale.

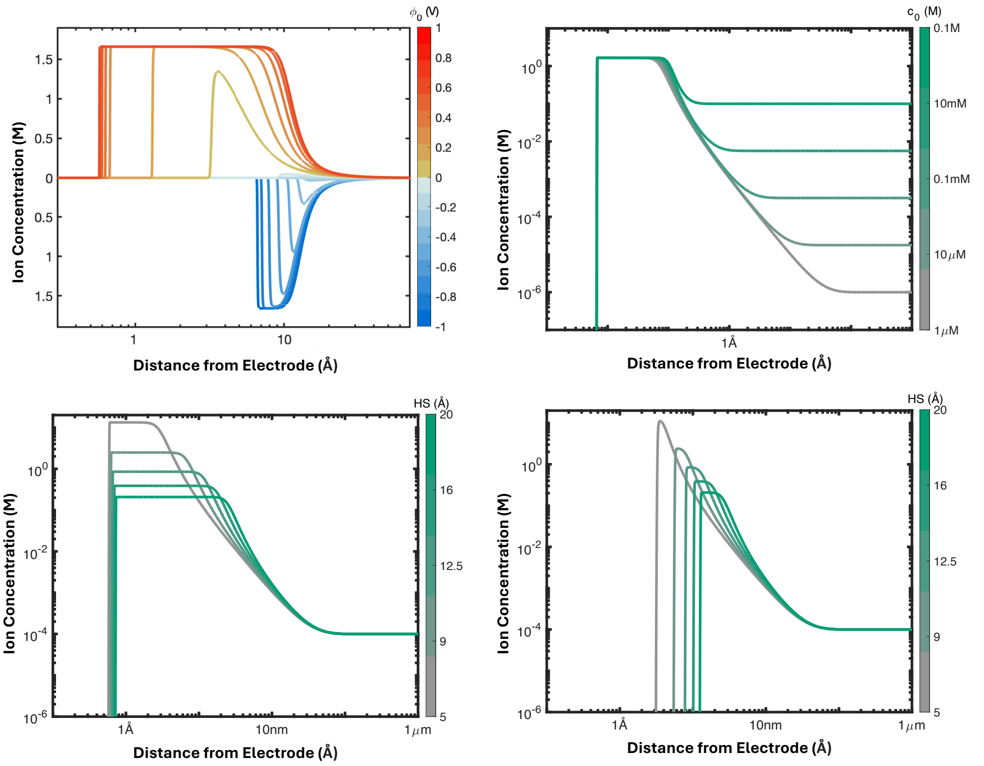

Fig. 3 Simulated profiles of ion distribution (a) with regard to electrode potential, (b) with regard to bulk concentration, (c) in anodic potential of 0.4V with regard to anion hydration shell size and (d) in cathodic potential of -0.4V with regard to cation hydration shell size

In Figure 3a, the ion distributions are plotted for various electrode potentials. For negative potentials, cations are attracted to the electrode surface, while for positive potentials, anions dominate near the surface. The Helmholtz layer thickness is generally greater for cations, corresponding to their hydration shell size. For anions, however, their stronger tendency to adsorb onto the surface results in a reduced Helmholtz layer thickness, approaching the radius of the bare ion. This behavior is also influenced by the electrode surface charge and the applied potential.

Within the compact layer, the ion concentration saturates at c_{max}, which is defined by the ion size. To form this compact layer, the electrode potential must exceed a certain threshold to attract the ions effectively.

Figure 3b illustrates the impact of bulk ion concentration. As expected, the bulk concentration does not affect the Helmholtz and compact layers. Instead, it primarily influences the Debye length in the diffusion layer, which becomes smaller with higher bulk concentrations, as clearly observed.

Figures 3c and 3d demonstrate the effects of hydration shell size for anions and cations, respectively. For anions, far from the potential of zero charge (PZC), the hydration shell size has little impact on the Helmholtz layer thickness. However, smaller anions allow for a higher $c_{\max}$, resulting in a greater concentration in the compact layer. In contrast, for cations, the Helmholtz layer thickness remains dependent on the hydration shell size, even at potentials far from the PZC. Smaller cations lead to a thinner Helmholtz layer, thinner compact layer, and, due to their higher $c_{\max}$, an increased ion concentration within the compact layer. Figure 4 illustrates the electric field at the interface. For negative potentials, the electric field is relatively lower due to the thinner Helmholtz layer. At high positive potentials, the electric field saturates near the electrode surface, as solvent molecules become fully oriented, resulting in a minimum relative permittivity in this region.

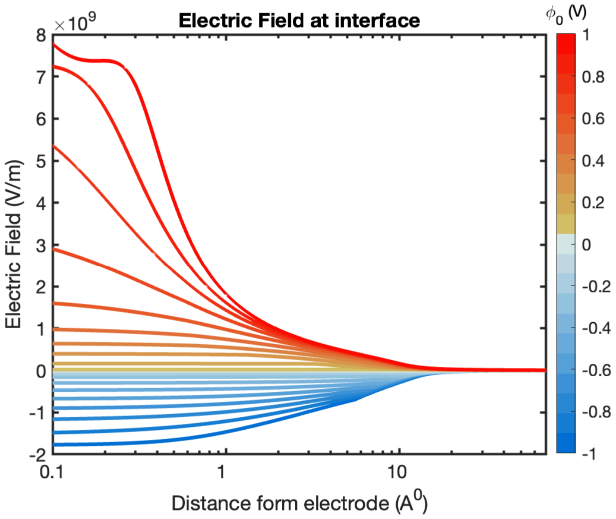

Fig. 4 Simulated profile of electric field at interface with regard to electrode potential

Figure 5 illustrates the simulated profiles of relative permittivity under different conditions. Figure 5a illustrates the relative permittivity as a function of electrode potential. The general trend shows that the relative permittivity increases from the electrode surface, where the electric field is strongest, to its maximum value in the bulk region. For cathodic potentials, the relative permittivity is lower compared to anodic potentials due to the stability of the one-H-down structure in the cathodic potential range.

Figure 5b presents the relative permittivity with respect to bulk ion concentration. Since bulk concentration does not significantly affect the Helmholtz and compact

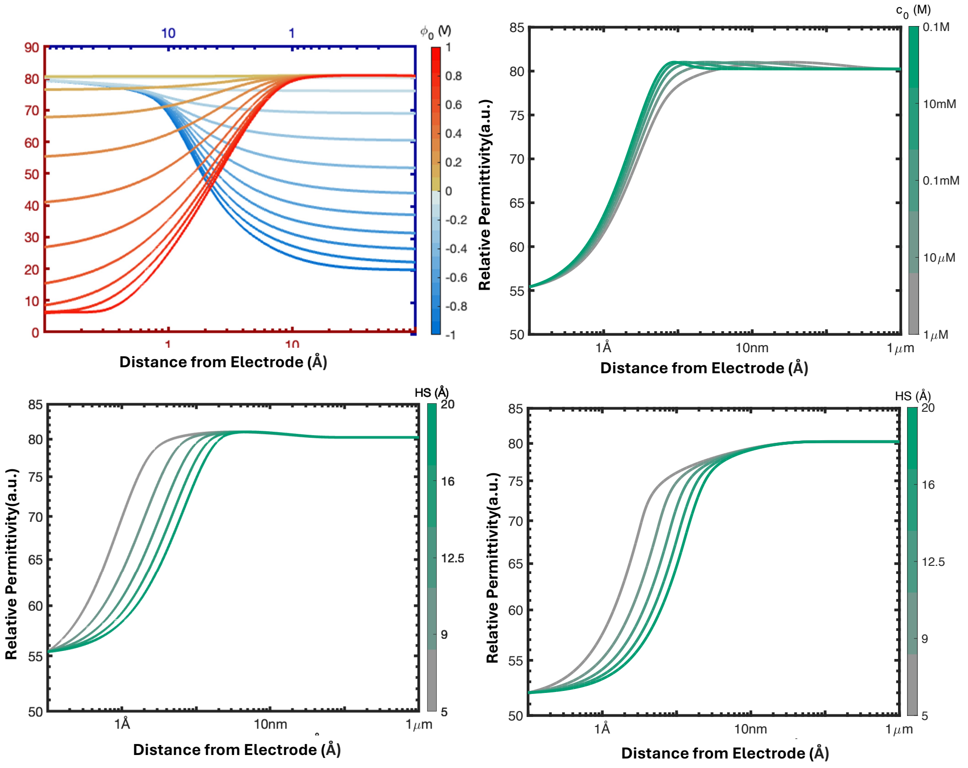

Fig. 5 Simulated profiles of relative permittivity: (a) with respect to electrode potential, where red and blue graphs represent permittivity at cathodic and anodic potentials, respectively (blue graphs are oriented from right to left on the top ruler). (b) with respect to bulk concentration, (c) with respect to anion hydration shell size at a potential of 0.4 V, and (d) with respect to cation hydration shell size at a potential of -0.4 V.

layers, differences appear primarily in the diffuse layer. At lower bulk concentrations, the diffuse layer is thicker, and the electric field decreases with a gentler slope. Consequently, the relative permittivity rises with a lower gradient in this region.

Figures 5c and 5d depict the relative permittivity as a function of anion and cation hydration shell sizes, respectively. Smaller ions result in a thinner compact layer and a higher ion concentration near the surface. This causes the electric field to decrease more sharply compared to the case of larger ions, which form a broader, lower-concentration compact layer. As a result, the relative permittivity increases with a steeper slope for smaller ions.

2 Impedance Model Overview

To model the impedance of the electrode interface, we assume the interface consists of multiple layers, each with its own capacitive and resistive behavior. Therefore, the interface can be treated as an infinite series of parallel resistors and capacitors. By summing the impedance of each layer, the total impedance of the interface can be calculated.

Generally, the capacitive behavior arises from both the solvent as the dielectric medium and the ion displacement. However, in this work, we neglect the capacitive contribution from ion displacement, as the AC potential amplitude in impedance measurements is typically below the thermal potential, which does not cause significant ion movement. We assume that ion distribution is only influenced by the electrode's DC potential. Consequently, the capacitance can be calculated based on the relative permittivity at each point, which is extracted from the mean-field model.

The resistance of each layer is determined by the conductivity of the dielectric medium and the ionic conductivity. In this work, we neglect the conductivity of water, as it is negligible compared to the conductivity of dissolved ions. However, it should be noted that this assumption does not hold at very low concentrations.

2.1 Ionic Conductivity

In dilute solutions, the conductivity of the electrolyte solution is the sum of the conductivities of the individual ions in the solution, which can be expressed as:

$$\sigma = \sum n_i q_i \mu_i \tag{11}$$

where n_i represents the number of free ions, q_i is the charge of the ion, and μ_i is the ion mobility.

Ion mobility refers to the average speed of ions under the influence of an electric field and results from the combined effects of the external electric field and the resistance to ion movement. When considering the ion and its associated hydration layer as a single entity, the resistance to ion movement during migration under the electric field includes contributions from ion-ion, ion-solvent, and solvent-solvent interactions. The ion-ion interaction is a long-range electrostatic force, while the ion-solvent and solvent-solvent forces are short-range interactions. At low concentrations, the long-range interactions dominate, and the short-range interactions are often neglected. However, as the electrolyte concentration increases, the distance between molecules decreases, and short-range interactions become significant, leading to a rapid increase in ion movement resistance. As a result, ion mobility typically decreases with increasing electrolyte concentration.

While the exact profiles of local ion conductivity and ion mobility are not fully known, we assume a simple exponential decay behavior between ion concentration and ion conductivity, based on the work by Zhang et al.[4] In their study, they modeled the overall conductivity of the electrolyte between two electrodes, rather than local conductivity. However, since ion mobility is expected to exhibit similar behavior at the local scale, we apply the same exponential decay profile for local conductivity.

The conductivity of the electrolyte solution is calculated using the following equation:

$$\sigma = Am \exp(-m/B) \tag{12}$$

where A corresponds to the ionic mobility at low concentrations, and B represents the collision effect that becomes significant at high concentrations.

Figure 6a demonstrates the general profile of conductivity as a function of ion concentration. In dilute solutions, the conductivity increases linearly with concentration. As the concentration reaches a point where ion-ion interactions begin to dominate, the conductivity starts to decrease. At very high concentrations, where the ions are at their maximum concentration, the conductivity approaches zero.

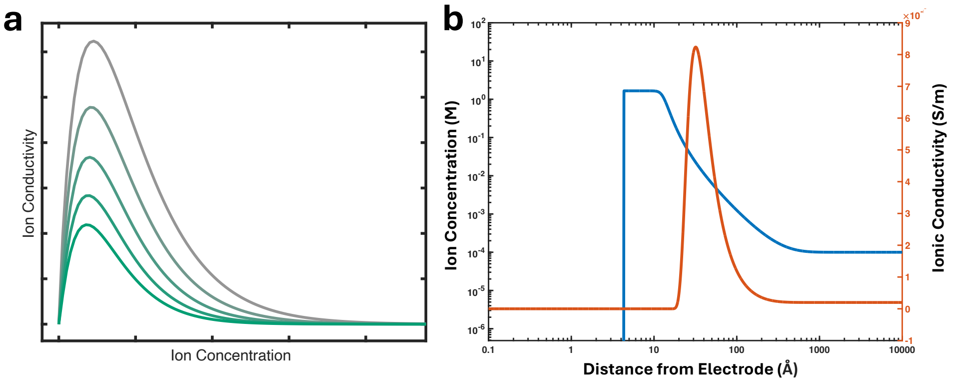

Fig. 6 (a) General trend of local ionic conductivity as a function of ion concentration, where the decay parameter is smaller for the greener curve, indicating a slower decline in conductivity. (b) Representative ionic conductivity profile at the interface compared to the corresponding ion concentration profile, highlighting the spatial variations in transport properties.

To calculate the resistance behavior of each layer, ion concentration data extracted from the mean-field model is used, and the equation 12 is applied to it. Figure 6b represents the general profile of conductivity at the interface. Starting from the electrode, the Helmholtz layer is depleted of ions, resulting in zero conductivity in this region. In the compact layer, although ions are present, the concentration reaches its maximum, leaving no space for ion movement; thus, the conductivity is again zero.

In the diffusion layer, the concentration begins to decrease, leading to fewer ion collisions and a rise in conductivity from zero. As we move further into the diffusion layer, conductivity continues to increase until it reaches its maximum value. This corresponds to the region where the concentration is still high.

Once the concentration decreases and enters the linear region of the conductivity-concentration profile, the conductivity begins to decrease as well, eventually reaching its bulk value.

2.2 Impedance Calculation

Figure 7 illustrates the flow diagram for the impedance calculation process. The first step involves providing input parameters, including ion parameters (hydration shell size and ion size), electrode potential, and bulk concentration, to the mean-field model. The model runs iteratively until it reaches the minimum error threshold defined for solving the differential equations. The output of the mean-field model, consisting of

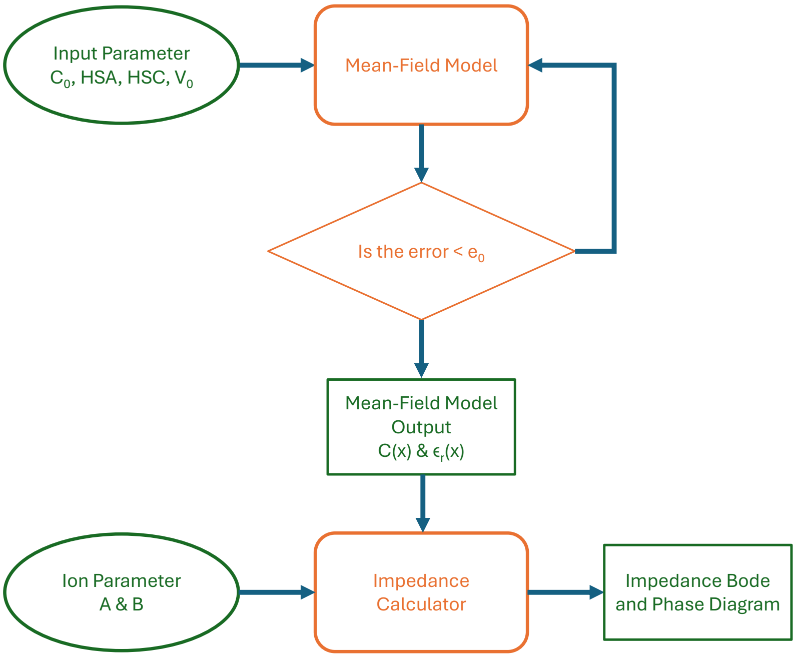

Fig. 7 Flow diagram of the impedance calculation process.

ion distribution and relative permittivity profiles, is used as input for the impedance calculator. The ion distribution determines the conductivity profile, while the permittivity profile is directly obtained from the mean-field model. The ion conductivity parameter(A and B) introduced to the model in this stage. The conductivity and permittivity in each layer of the interface are determined.

The impedance of each infinitesimal layer is calculated as follows:

$$z_{dx} = \frac{dx}{\sigma + j \cdot \omega \epsilon_0 \epsilon_r}, \tag{13}$$

where σ is the conductivity, ϵ_0 is the vacuum permittivity, ϵ_r is the relative permittivity and ω is the angular frequency.

The frequency range for the calculations is set between 1 mHz and 100 MHz. By summing the impedance of all layers, the total impedance of the interface is determined:

$$Z = \int_0^L z_{dx}\, dx, \tag{14}$$

where L is the total thickness of the interfacial region.

2.3 Impedance Calculation Validation

To validate the impedance calculator, Bode and phase diagrams under specific conditions have been analyzed. For example, the bulk conductivity is expected to result in lower impedance. Figure 8 illustrates the Bode and phase diagrams of the interface with respect to varying bulk concentrations.

As anticipated, the interface impedance decreases with higher bulk conductivity, particularly in the middle-frequency range. The general impedance profile demonstrates three distinct behaviors:

- Low frequencies: A capacitive behavior dominates, attributed to the capacitance of the Helmholtz, compact, and diffusion layers.
- Middle frequencies: A resistive behavior emerges, caused by conduction in the bulk layer.
- High frequencies: Another capacitive behavior is observed, resulting from the natural dielectric behavior of water.

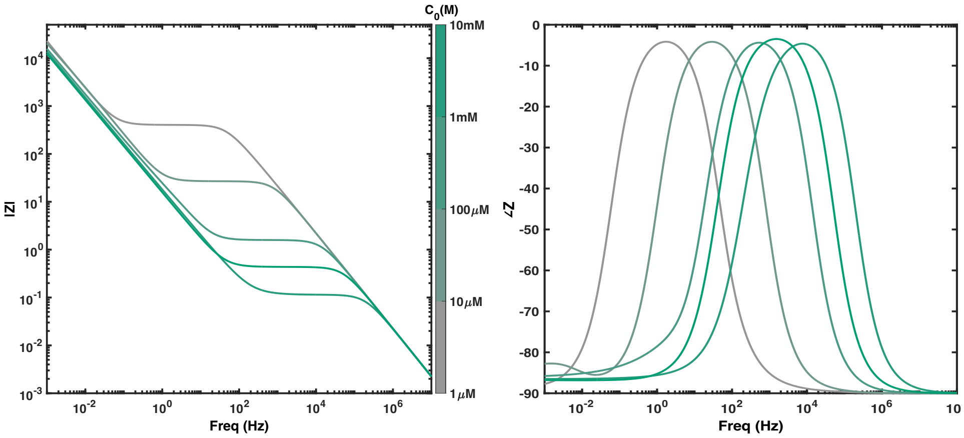

Fig. 8 Bode and phase diagrams of the interface with varying bulk concentrations.

An increase in ion mobility primarily reduces the resistance in the bulk layer, leading to lower impedance in the medium-frequency range. Figure 9 illustrates the interface impedance as a function of the ionic mobility parameter (A).

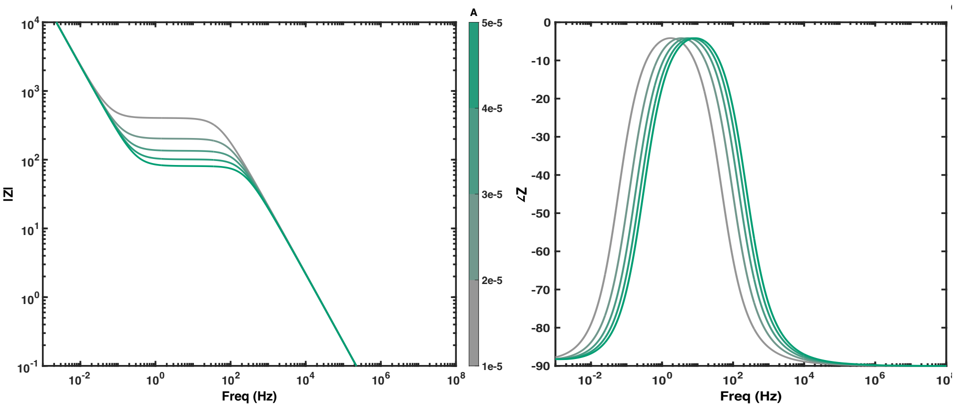

Fig. 9 Bode and phase diagrams of the interface with varying ion mobility.

3 Experimental Setup and Configuration

For the experimental measurements, commercially available salts were purchased and dissolved in distilled water to prepare the electrolyte solution. The measurements were conducted using a fabricated microelectrode on a silicon substrate. The electrode configuration is shown in Figure 10a. An interdigital design was utilized to maximize the electrode surface area while maintaining a minimal electrode spacing of 10 μm. This design helps to reduce the impedance contribution of the bulk layer. The electrodes were fabricated to achieve a flat surface with a roughness of less than 5 nm. This ensures uniform electric field distribution and minimizes measurement artifacts caused by surface irregularities. During the experiments, the temperature was precisely controlled at 25°C using an active thermal bath. To reduce environmental noise, the entire system was enclosed in a Faraday cage. The experimental setup is illustrated in Figure 10b.

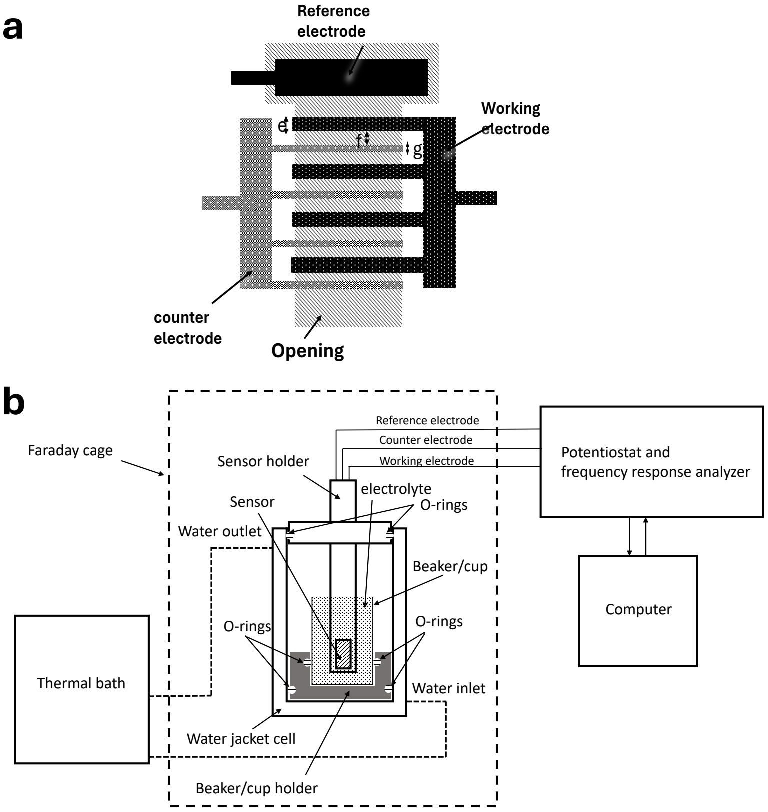

Fig. 10 (a) Electrode configuration with interdigital design for enhanced surface area and minimized bulk layer impedance. (b) Experimental setup showing the thermal bath and Faraday cage for environmental noise reduction.

EIS measurements were performed over a frequency range of 10 mHz to 7 MHz in single-sine mode. Each frequency point was measured three times, ensuring robust data collection, with a total measurement time of approximately 30 minutes. Prior to each EIS measurement, the open circuit potential (OCP) of the electrochemical cell was recorded for 30 minutes to ensure system stability.

To validate data accuracy, a control measurement using distilled water was conducted before and after each experimental run. This step was essential to detect any contamination of the electrode. If contamination was observed, the electrodes were cleaned using RCA1 and RCA2 cleaning procedures before repeating the measurement.

To assess reproducibility, each EIS measurement was repeated three times under identical conditions. The error between measurements was calculated using the following equation:

$$\text{Error (\%)} = \frac{|Z_1 - Z_2|}{Z_{\text{avg}}} \times 100 \tag{15}$$

where Z_1 and Z_2 are the impedance values from two measurements, and Z_{avg} is their average. If the calculated error exceeded 3%, the measurement was excluded from the dataset to ensure the reliability and quality of the data.

4 ML-Based Model Overview

In this section, we provide detailed information necessary to reproduce the prediction model.

4.1 Output: Encoding of Solute and Concentration

The electrochemical impedance dataset obtained from experiments comprises 536 valid samples, covering nine solute types and 16 concentration levels. Each solution contains one, two, or three different solutes. The dataset includes the cations Zn^{2+}, Cd^{2+}, and Pb^{2+}, as well as the anions NO_3^-, SO_4^{2-}, and Cl^-. The concentration of a single solute ranges from 100 nmol/L to 10 mmol/L.

To determine the cations, anions, and their respective concentrations from the impedance curves, we employ a machine learning approach. The ML model predicts a six-dimensional output where each value denotes an ion concentration as per the following ordering scheme: Zn^{2+}, Cd^{2+}, Pb^{2+}, $(NO_3)^-$, Cl^-, SO_4^{2-}. Given the broad range of concentration values, the concentration c is normalized using the following transformation:

$$c_{\text{nor}} = \begin{cases} \log(c), & \text{if} \quad c > 0, \\ -20, & \text{otherwise}, \end{cases} \tag{16}$$

where c_{nor} represents the normalized concentration. The distribution of unnormalized and normalized concentration encodings are illustrated in Fig. 11.

4.2 Input: EIS Data

Our machine learning model processes impedance data to identify the solution composition. The frequency of the impedance curve is uniformly sampled from the frequency

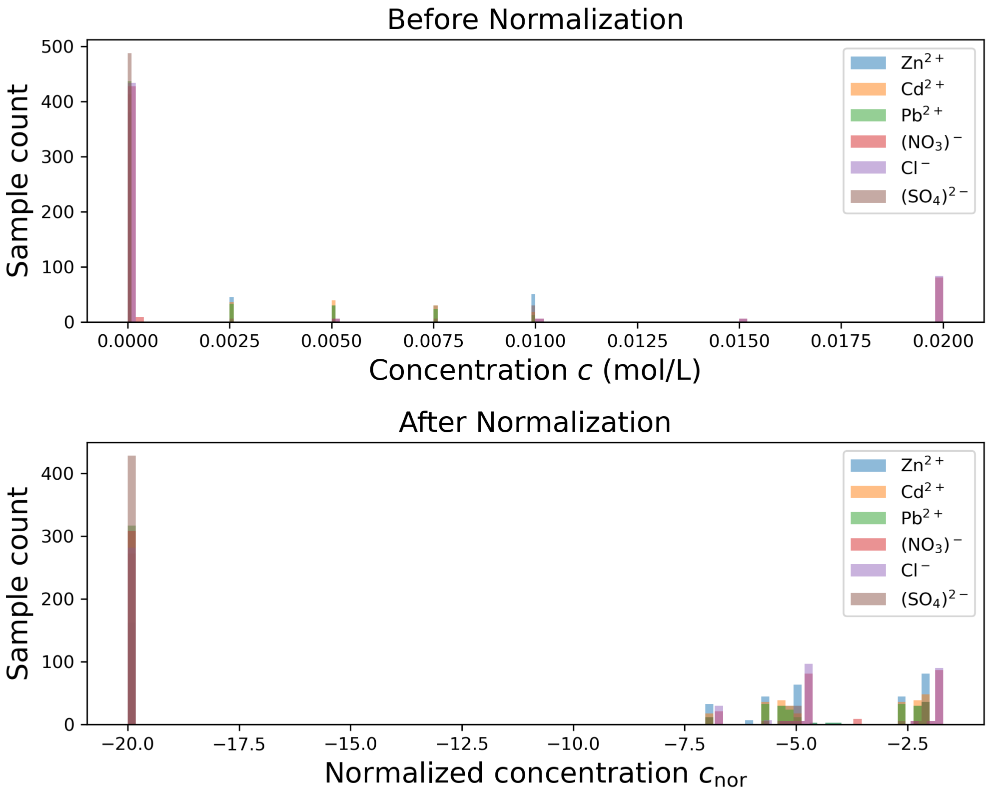

Fig. 11 Distribution of the concentrations before and after normalization.

range 1 MHz to 100 MHz and consists of 50 equally spaced feature points. The entries of this 50-dimensional feature vector are referred to by their positional "Index" in the subsequent discussion. To adapt the input curve for the machine learning framework, the following transformation steps are applied: (i) Let $X = \log \mathrm{Re}(Z) + i \log \mathrm{Im}(Z)$ denote the impedance curve, where $\mathrm{Re}(Z)$ and $\mathrm{Im}(Z)$ are the real and imaginary components of the impedance Z, respectively, and i is the imaginary unit. To improve the distribution properties of the data, a Power Transformer function F [5, 6] is applied to both components, yielding: $T = F[\log \mathrm{Re}(Z)] + iF[\log \mathrm{Im}(Z)]$. This transformation makes the data more Gaussian-like, as illustrated in Fig. 12. The normalization enhances separability between samples, ultimately improving feature recognition in the machine learning model. (ii) The normalized real and imaginary feature vectors of the impedance data are concatenated to obtain a 100-dimensional feature vector. A Fourier transform is applied to this 100-dimensional vector to extract frequency-domain features. (iii) Principal component analysis (PCA) is performed on the amplitude spectrum of the fourier transform of the 100-dimensional feature vector to capture the most significant features. We retain 20 principal components, which together explain 99.99% of the total variance. This reduces the input dimensionality to 20, optimizing the representation for the machine learning model.

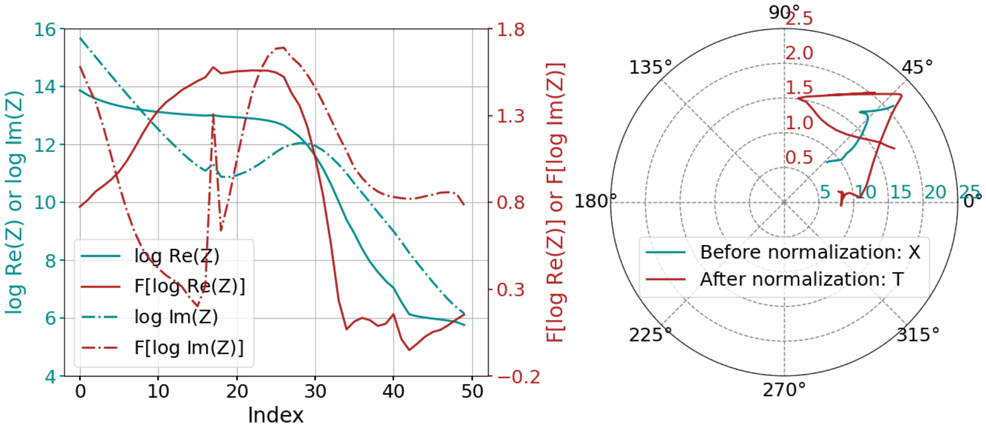

Fig. 12 Example of impedance data represented in both Cartesian and polar coordinates.

4.3 Predicting Ion Concentrations

A total of 536 samples are randomly split into a training dataset (90%) and test dataset (10%). A Multi-layer Perceptron (MLP) model with input dimension 20 and output dimension 6 is established. The architecture of the MLP is shown in Fig. 13. To avoid overfitting, dropout layers are added to the neural network. Training protocols for the MLP model are given in Table 1. Loss curves is shown in Fig. 14. R^2 plots for all ions are shown in Fig. 15. Several typical examples are shown in Fig. 16.

Table 1 Training protocols for the MLP model.

	MLP
Hidden layer dimensions	200, 200, 200, 100, 100
Activation functions	no activation for output layer; ReLU otherwise
Optimizer	Adam
Learning rate	0.001
Number of epochs	40000
Dropout	0.05, 0.05, 0, 0, 0
Software	Pytorch
Hardware	CPU
Runtime	5 minutes

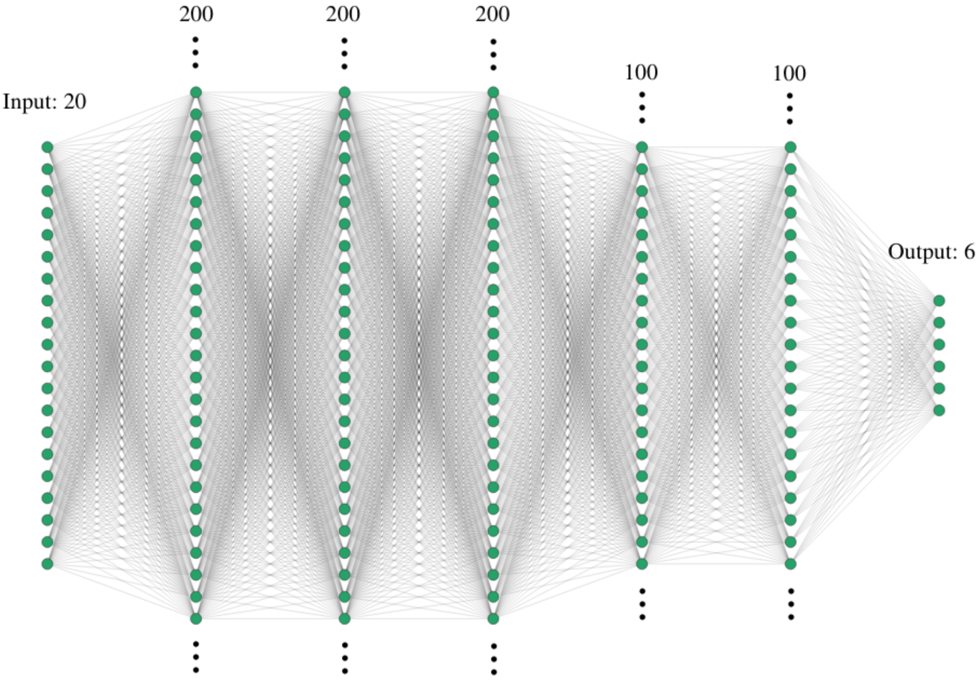

Fig. 13 Architecture of the MLP model. The dimension of each input, output, or hidden layer is denoted by the number above it.

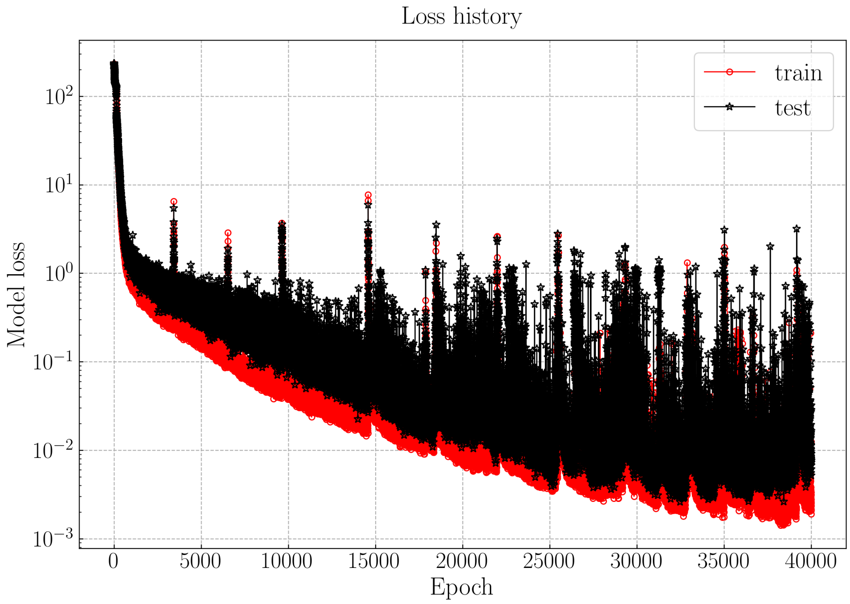

Fig. 14 Loss history on training and test dataset.

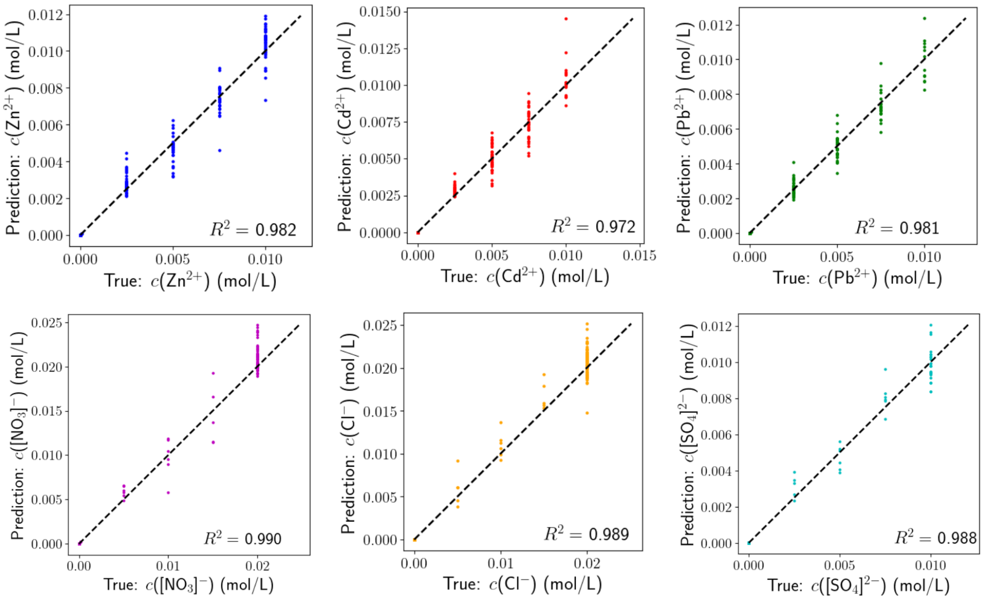

Fig. 15 Predicted (via the ML model) vs. true concentrations in the test dataset. All dashed lines represent the ideal line with zero-intercept and unit-slope; the corresponding R^2 goodness-of-fit are indicated.

(a) Training set

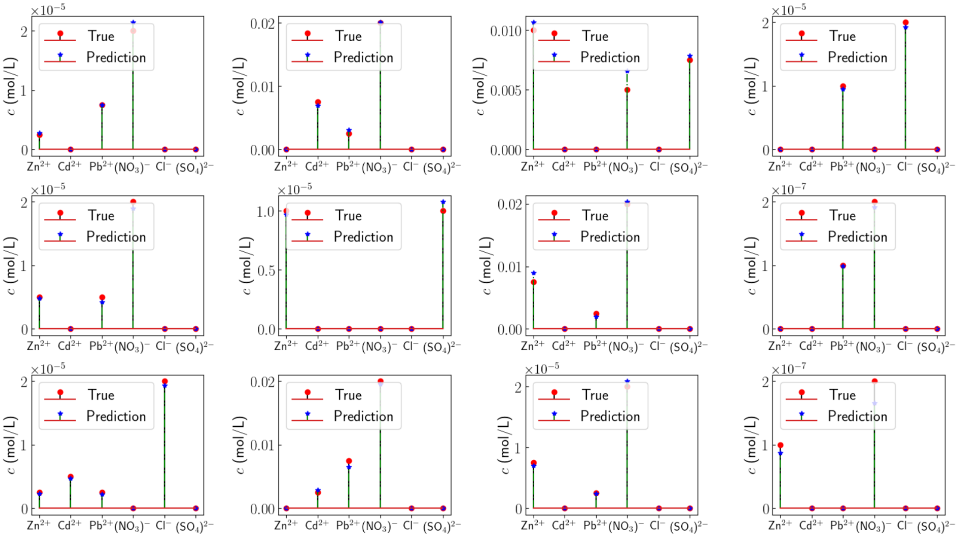

(b) Test set

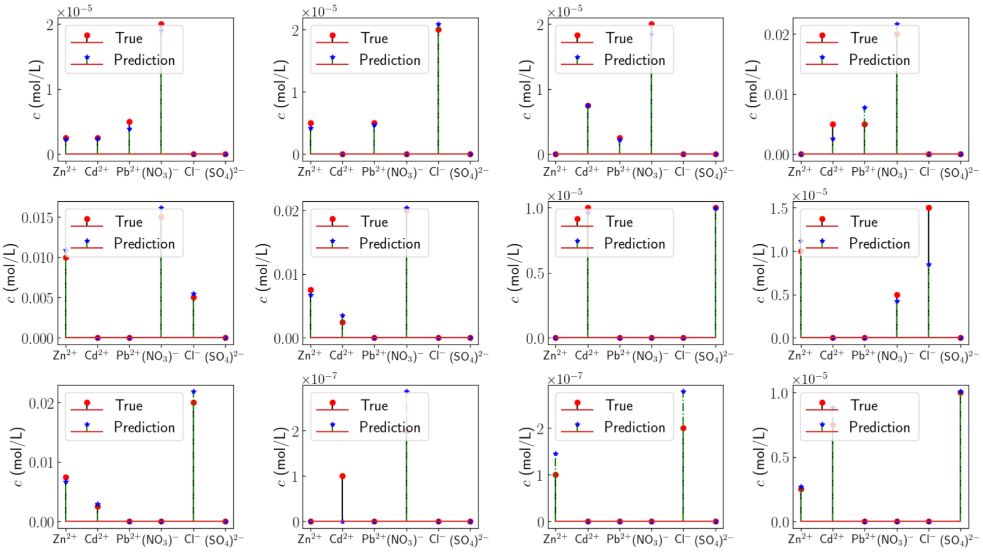

Fig. 16 A gallery of 24 representative examples comparing predicted solutions with true solutions on (a) the training set and (b) the test set. Agreement between the true and predicted solutions demonstrates the accuracy of the ML model.

5 Modeling Parameters

A detailed summary of the model parameters and their corresponding values for each figure is presented in Table 2. We believe that This information is sufficient for replicating the numerical and analytical results described in the main text.

Parameter	**Unit**	**Figure 1b**	**Figure 1c**	**Figure 2a-c**	**Figure 2d**	**Figure 3a&b**
L	μm	0.42	0.42	0.42	0.6	0.42
hs_{an}	Å	4	4	4	3	3.7
hs_{ca}	Å	3.6	3.6	3.6	1–5	3.7
r_{an}	Å	1.7	1.7	1.7	0.5	0.5
r_{ca}	Å	1	1	1	0.5	0.5
z_{an}	a.u.	-1	-1	-1	-2	-2
z_{ca}	a.u.	1	1	1	2	2
c_0	mol L^{-1}	1.00E-02	1.00E-02	1.00E-02	5.00E-03	1.00E-02
V_0	V	-1–1	-1–1	-1–1	-0.25	-0.5
A	S/m	–	–	5.00E-03	5.00E-03	5.00E-01
B	mo L^{-1}	–	–	0.01	$C_{\max}/\log(10^{-25}/A.C_{\max})$	0.3–0.5
f	Hz	–	–	10^{-3}–10^{8}	10^{-3}–10^{8}	10^{-3}–10^{8}

Table 2 Model Parameters and Their Values main text Figures

References

[1] Doblhoff-Dier, K., Koper, M.T.M.: Modeling the gouy–chapman diffuse capacitance with attractive ion–surface interaction. The Journal of Physical Chemistry C **125**(30), 16664–16673 (2021) https://doi.org/10.1021/acs.jpcc.1c02381

[2] Le, J.-B., Fan, Q., Li, J., Cheng, J.-B.: Molecular origin of negative component of helmholtz capacitance at electrified pt(111)/water interface. Science Advances **6**(44), 1219 (2020) https://doi.org/10.1126/sciadv.abb1219

[3] Shin, S.J., Kim, D.H., Bae, G., *et al.*: On the importance of the electric double layer structure in aqueous electrocatalysis. Nature Communications **13**, 174 (2022) https://doi.org/10.1038/s41467-021-279

[4] Zhang, W., Chen, X., Wang, Y., Wu, L., Hu, Y.: Experimental and modeling of conductivity for electrolyte solution systems. ACS Omega **5**(35), 22465–22474 (2020) https://doi.org/10.1021/acsomega.0c03013

[5] Pedregosa, F., Varoquaux, G., Gramfort, A., Michel, V., Thirion, B., Grisel, O., Blondel, M., Prettenhofer, P., Weiss, R., Dubourg, V., Vanderplas, J., Passos, A., Cournapeau, D., Brucher, M., Perrot, M., Duchesnay, E.: Scikit-learn: Machine learning in Python. Journal of Machine Learning Research **12**, 2825–2830 (2011)

[6] Yeo, I., Johnson, R.A.: A new family of power transformations to improve normality or symmetry. Biometrika **87**(4), 954–959 (2000) https://doi.org/10.1093/biomet/87.4.954 https://academic.oup.com/biomet/article-pdf/87/4/954/633221/870954.pdf